Planarizing cytosine: The S_1 state structure, vibrations, and nonradiative dynamics of jet-cooled 5,6-trimethylenecytosine

Maria A. Trachsel, Simon Lobsiger, Tobias Schär, Lluís Blancafort, and Samuel Leutwyler

Citation: The Journal of Chemical Physics **146**, 244308 (2017);
View online: https://doi.org/10.1063/1.4989465
View Table of Contents: http://aip.scitation.org/toc/jcp/146/24
Published by the American Institute of Physics

Planarizing cytosine: The S_1 state structure, vibrations, and nonradiative dynamics of jet-cooled 5,6-trimethylenecytosine

Maria A. Trachsel,[1] Simon Lobsiger,[1] Tobias Schär,[1] Lluís Blancafort,[2,a)] and Samuel Leutwyler[1,b)]

[1]*Department of Chemistry and Biochemistry, University of Bern, Freiestrasse 3, CH-3012 Bern, Switzerland*
[2]*Institut de Química Computacional i Catàlisi and Departament de Química, Facultat de Ciències, Universitat de Girona, C/M. A. Campmany 69, 17003 Girona, Spain*

(Received 17 February 2017; accepted 9 June 2017; published online 26 June 2017)

We measure the $S_0 \rightarrow S_1$ spectrum and time-resolved S_1 state nonradiative dynamics of the "clamped" cytosine derivative 5,6-trimethylenecytosine (TMCyt) in a supersonic jet, using two-color resonant two-photon ionization (R2PI), UV/UV holeburning, and ns time-resolved pump/delayed ionization. The experiments are complemented with spin-component scaled second-order approximate coupled cluster (SCS-CC2), time-dependent density functional theory, and multi-state second-order perturbation-theory (MS-CASPT2) *ab initio* calculations. While the R2PI spectrum of cytosine breaks off ~500 cm^{-1} above its 0_0^0 band, that of TMCyt extends up to +4400 cm^{-1} higher, with over a hundred resolved vibronic bands. Thus, clamping the cytosine C^5–C^6 bond allows us to explore the S_1 state vibrations and $S_0 \rightarrow S_1$ geometry changes in detail. The TMCyt S_1 state out-of-plane vibrations ν'_1, ν'_3, and ν'_5 lie below 420 cm^{-1}, and the in-plane ν'_{11}, ν'_{12}, and ν'_{23} vibrational fundamentals appear at 450, 470, and 944 cm^{-1}. $S_0 \rightarrow S_1$ vibronic simulations based on SCS-CC2 calculations agree well with experiment if the calculated ν'_1, ν'_3, and ν'_5 frequencies are reduced by a factor of 2–3. MS-CASPT2 calculations predict that the ethylene-type $S_1 \rightsquigarrow S_0$ conical intersection (CI) increases from +366 cm^{-1} in cytosine to >6000 cm^{-1} in TMCyt, explaining the long lifetime and extended $S_0 \rightarrow S_1$ spectrum. The lowest-energy $S_1 \rightsquigarrow S_0$ CI of TMCyt is the "amino out-of-plane" (OP_X) intersection, calculated at +4190 cm^{-1}. The experimental $S_1 \rightsquigarrow S_0$ internal conversion rate constant at the $S_1(v' = 0)$ level is $k_{IC} = 0.98\text{–}2.2 \cdot 10^8$ s^{-1}, which is ~10 times smaller than in 1-methylcytosine and cytosine. The $S_1(v' = 0)$ level relaxes into the $T_1(^3\pi\pi^*)$ state by intersystem crossing with $k_{ISC} = 0.41\text{–}1.6 \cdot 10^8$ s^{-1}. The T_1 state energy is measured to lie 24 580 ± 560 cm^{-1} above the S_0 state. The $S_1(v' = 0)$ lifetime is $\tau = 2.9$ ns, resulting in an estimated fluorescence quantum yield of $\Phi_{fl} = 24\%$. Intense two-color R2PI spectra of the TMCyt amino-enol tautomers appear above 36 000 cm^{-1}. A sharp S_1 ionization threshold is observed for amino-keto TMCyt, yielding an adiabatic ionization energy of 8.114 ± 0.002 eV. [http://dx.doi.org/10.1063/1.4989465]

I. INTRODUCTION

A number of femtosecond (fs) pump-probe studies of cytosine (Cyt), 1-methylcytosine (1-MCyt), and 5-fluorocytosine (5-FCyt) in the gas-phase have yielded ultrashort excited-state S_1 lifetimes that range from $\tau = 0.2$ to 3.2 ps.[1–5] However, more recent measurements of supersonically jet-cooled amino-keto Cyt, 5-methylcytosine (5-MCyt), and 5-FCyt based on Lorentzian lifetime broadening measurements at their respective $S_0 \rightarrow S_1$ electronic origins yielded lower limits on the S_1 lifetimes of 45 ps for Cyt and 75 ps for 5-FCyt.[6–8] More recent direct lifetime measurements of Cyt, 1-MCyt, and 1-ethylcytosine (1-ECyt) using the picosecond (ps) excitation/ionization delay technique revealed even longer values between τ = 450–900 ps, which decrease rapidly with increasing vibrational excess energy (E_{exc}).[9]

Computational studies of the excited-state dynamics and nonradiative decay of amino-keto Cyt[10–20] have located three different conical intersections (CIs) between the ground and lowest excited $^1\pi\pi^*$ states. The lowest of these, which dominates the $S_1 \rightsquigarrow S_0$ nonradiative decay, is called $(Eth)_X$ since the intersection structure is similar to the CI structure of ethylene. This CI is characterized by a puckering of the C^6 atom and a twist around the C^5–C^6 bond, with a H–C^5–C^6–H torsional angle of ~120°.[10–13,15,16,19,21,22] The next higher CI involves an N^3 out-of-plane bending and a large out-of-plane amino deformation and is called $(OP)_X$.[10,16,19,22] The third CI, called $(n_O, \pi^*)_X$, has a semi-planar structure with sp^3 hybridization of the C^6 atom, shortening of the C^2–N^3 bond, and stretching of the C^2-O bond relative to the ground state minimum.[10–16,19,21,22]

Zgierski *et al.* have shown that covalently clamping the C^5–C^6 bond of Cyt with a trimethylene bridge in 5,6-trimethylenecytosine (TMCyt) increases the S_1 state fluorescence lifetime and quantum yield in room-temperature

a)E-mail: lluis.blancafort@udg.edu
b)E-mail: leutwyler@dcb.unibe.ch

aqueous solution by ~1000 times relative to Cyt,[23–25] to τ = 1.2 ns and Φ_{fl} ~ 10%.[26] Their configuration interaction singles (CIS) and second-order approximate coupled cluster (CC2) excited-state calculations predicted that this clamping shifts the $(Eth)_X$ conical intersection of cytosine to ~1500 cm^{-1} above the S_1 minimum, making this CI energetically less accessible.[26] The trimethylene bridge in TMCyt hardly affects the π-electron framework of Cyt, so the $S_0 \rightarrow S_1$ absorption band shifts from λ_{max} = 267 nm for Cyt to 280 nm in TMCyt.[26] In the clamped cytosine derivative pyrrolocytosine (PC), the C^4-amino group (see Fig. 1) and the C^5 atom are covalently connected, resulting in a pyrrole ring fused to the Cyt chromophore.[27] This extension of the π-electron framework significantly shifts the $S_0 \rightarrow S_1$ excitation maximum to λ_{max} = 330–345 nm, or about 70–80 nm to the red, compared to Cyt.[28,29] For PC, Thompson and co-workers have measured a lifetime of τ = 2.9 ns and a quantum yield of Φ_{fl} ~ 0.038 in pH 7 phosphate buffer.[29]

Intrigued by these observations, we have measured and analyzed the $S_0 \rightarrow S_1$ vibronic spectrum of supersonic jet-cooled TMCyt using two-color resonant two-photon ionization (2C-R2PI), UV/UV holeburning, and depletion spectroscopies. We also measured the S_1 state lifetime and triplet-state formation kinetics as a function of E_{exc}, using the nanosecond excitation/ionization delay technique, and report S_1 state nonradiative rate constants for internal conversion and intersystem crossing. In addition to the amino-keto tautomer **1** of TMCyt, we have also observed an intense R2PI spectrum that we assign to the $S_0 \rightarrow S_1$ transitions of the hydroxy-enol tautomers **2a/2b**, see Fig. 1 for the tautomer structures. The measurements are accompanied by calculations of the lowest excited singlet ($^1\pi\pi^*$) and triplet ($^3\pi\pi^*$) states of TMCyt using time-dependent (TD) density functional theory (DFT) (TD-CAMB3LYP), spin-component scaled CC2 (SCS-CC2),

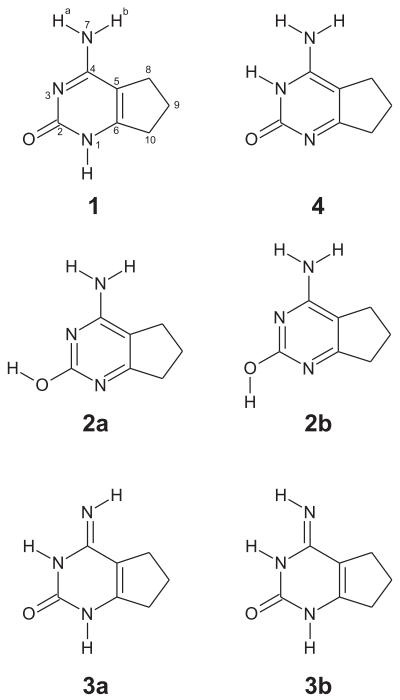

FIG. 1. The six most stable tautomers of gas-phase 5,6-trimethylenecytosine. The cytosine tautomer labels are analogous to that defined in Ref. 45.

complete-active-state self-consistent field (CASSCF), and multi-state second-order perturbation-theory (MS-CASPT2) methods.

II. METHODS

A. Experimental methods

TMCyt was synthesized in three steps from adiponitrile according to Ref. 30 and characterized by ^{1}H-NMR spectroscopy, ^{13}C-NMR spectroscopy, and electrospray ionization (ESI) mass spectrometry as described in the supplementary material. The experimental setup for two-color resonant two-photon ionization (2C-R2PI) measurements has been previously described.[31,32] Neon carrier gas at ~1.8 bar backing pressure was passed through a 20 Hz pulsed nozzle (0.4 mm diameter) heated to 230 °C that contains the TMCyt sample. 2C-R2PI spectra were measured by crossing the skimmed supersonic jet with the unfocused UV excitation and ionization laser beams in the source of a linear time-of-flight mass spectrometer (TOF-MS). Excitation was performed with 0.4–0.6 mJ UV pulses from a frequency-doubled Radiant Dyes NarrowScan D-R dye laser with a bandwidth of 0.05 cm^{-1} (1500 MHz) or with an Ekspla NT342B optical parametric oscillator (UV-OPO) with a bandwidth of 4–6 cm^{-1}. The frequency scale was calibrated by measuring the fundamental frequency with the WS6 wavemeter.

Ionization light of ~100 μJ/pulse at 225 or 245 nm was produced by an Ekspla NT342B (UV-OPO). The measurements were typically done with 10–30 mV ion signal at the most intense vibronic band. A second frequency-doubled dye laser (~400 μJ/pulse) was used as the UV-depletion laser for UV/UV holeburning and depletion experiments. Excitation and ionization were performed as for the R2PI experiments. The depletion laser was fired 300 ns before the excitation/ionization laser pulses.

B. Computational methods

A uniform theoretical treatment of the ground- and excited-state potential energy surfaces of TMCyt is difficult, and we have combined several methods following a similar approach to our recent work on 1-MCyt.[33] The electronic ground state of all 14 tautomers and rotamers of TMCyt was first optimized using density functional theory (B3LYP) with the TZVP basis set. The ground state structures of the six most stable tautomers are shown in Fig. 1; these were re-optimized at the correlated level, using the second-order Møller-Plesset (MP2) method in the resolution-of-identity (RI) approximation, the SCS-MP2 method, and the CC2 method in the RI approximation, using the aug-cc-pVTZ basis set.

The adiabatic and vertical transition energies were calculated at the SCS-CC2 level of theory with the aug-cc-pVDZ basis set. Normal-mode calculations were performed for all geometry-optimized structures to assure that they correspond to true potential energy surface minima. The transition energies were also calculated at the MS-CASPT2 level of theory. For the $\pi\pi^*$ and $^1n_O\pi^*$ states, we used TD-CAM-B3LYP/6-311G** optimized geometries, whose MS-CASPT2 energy is lower than that of their CASSCF and SCS-CC2 analogues. For the optimization of $(OP)_{Min}$, we used the CASSCF(12,12)/

6-311G** geometry because the other methods failed to converge to a minimum for that state.

For the calculation of the decay paths and conical intersections, we follow the MS-CASPT2//CASSCF approach, where the paths and structures are optimized at the CASSCF level of theory and the energy profiles along the paths are recalculated at the MS-CASPT2 level to include dynamic correlation energy (see our previous study of 1-MCyt[33]). For the CASSCF and MS-CASPT2 calculations, we used, respectively, the 6-311G** basis and the ANO-L basis set contracted to 4s3p2d for C, N, and O and 3s2p1d for H. For the CASPT2 calculations, we used an imaginary level shift[34] of 0.1 a.u. and the standard ionization potential–electron affinity correction[35] of 0.25 a.u.

To calculate the reaction path to $(OP)_X$, we optimized the transition structure (TS) on S_1 and obtained the path by combining the intrinsic reaction coordinate[36] and initial relaxation direction[37] techniques. The calculated barrier includes the vibrational zero-point energy (ZPE) correction, which amounts to −475 cm^{-1}, based on CASSCF frequencies at $(^1\pi\pi^*)_{Min}$ (with $3N - 6$ vibrational modes) and at the corresponding TS (including $3N - 7$ modes). The CI was optimized using the recently developed double Newton-Raphson algorithm.[38] The active space of the CASSCF and MS-CASPT2 calculations was specifically tailored for each path; for details, see the supplementary material. We use (10,10) and (12,12) active spaces for the ethylene- and OP-type paths, respectively. With this approach, the MS-CASPT2 S_1/S_0 energy gaps at the CI structures were 1973 and 2265 cm^{-1} (0.24 and 0.28 eV) at $(Eth)_X$ and $(OP)_X$, respectively. The path to $(Eth)_X$, which has a sloped topology and does not involve a TS, was approximated with a linear interpolation in internal coordinates.

Density functional theory and CC2 calculations were performed using Turbomole 6.4.[39,40] The CASSCF optimizations were performed with a modified version of Gaussian09[41] and the MS-CASPT2 calculations with Molcas 7.8.[42,43] Vibronic band simulations were done with the PGOPHER program.[44] As inputs, we used the SCS-CC2 calculated S_0 ground and S_1 excited state geometries and the corresponding normal-mode l matrices, employing conformer **1a**. Additional diagonal anharmonicity constants[44] were included for some modes. The vibronic band intensities are based on full multidimensional Franck-Condon factors, including both mode displacements and mixing between modes (Dushinsky effect).[44] The vibronic simulations for conformer **1b** are very similar to those for **1a**.

III. RESULTS AND DISCUSSION

A. Computational results

1. Tautomers and relative energies

Figure 1 shows the six most stable calculated tautomers and rotamers of TMCyt, and Table I summarizes their relative energies calculated at different levels of theory. All the correlated wave function methods predict the *trans*-amino-enol **2b** tautomer to be the most stable one, with the corresponding *cis*-rotamer **2a** ∼ 0.6 kcal/mol higher. The amino-keto N1H tautomer **1** that is experimentally investigated below exists in conformer **1a**, where the amino group and trimethylene ring are out-of-plane in the same direction, denoted Up-up (or Down-down), where the first (capitalized) orientation refers to the NH_2 group. In conformer **1b**, the NH_2 group and trimethylene ring are arranged in opposite directions (Up-down or Down-up). The **1a** and **1b** forms are close in energy with **1b** calculated to lie 3–4 cm^{-1} above **1a**. In the gas phase, both **1a** and **1b** are less stable than amino-enol conformers by 1.08 kcal/mol (CC2) or 1.54 kcal/mol (SCS-MP2). The B3LYP density functional method predicts the amino-keto N1H tautomer to be the most stable tautomer; however, it is known that this method predicts the order of the cytosine tautomers incorrectly.[6,45]

TABLE I. Calculated relative energies (in kcal/mol) of 5,6-trimethylene-cytosine tautomers and rotamers (see Fig. 1 for definitions). The bold font indicates the most stable (lowest energy) tautomer/rotamer.

	B3LYP TZVP	MP2 aVTZ	CC2 aVTZ	SCS-MP2 aug-cc-pVTZ
Amino-keto N1H (**1a**)	**0.00**	2.69	1.08	1.54
Amino-keto N1H (**1b**)	0.02	2.69	1.09	1.55
Amino-enol-*trans* (**2b**)	0.42	**0.00**	**0.00**	**0.00**
Amino-enol-*cis* (**2a**)	1.01	0.56	0.57	0.57
Imino-keto-*trans* (**3a**)	0.58	2.87	2.05	0.60
Imino-keto-*cis* (**3b**)	2.20	4.55	3.68	2.20
Amino-keto N3H (**4**)	5.52	8.46	6.64	7.39
Imino-enol-*cis-trans* N1H	27.8			
Imino-enol-*cis-cis* N1H	18.2			
Imino-enol-*trans-trans* N1H	32.5			
Imino-enol-*trans-cis* N1H	21.9			
Imino-enol-*cis-trans* N3H	15.4			
Imino-enol-*cis-cis* N3H	24.6			
Imino-enol-*trans-trans* N3H	12.5			
Imino-enol-*trans-cis* N3H	20.6			

The other TMCyt tautomers **2b**, **2a**, and **4** also exist as pairs of conformers analogous to **1a/1b**, but only one form was calculated since the energy difference is expected to be very small. All the imino-enol forms lie >13 kcal/mol above the most stable tautomer **2b** at the B3LYP/TZVP level; hence, we do not consider them any further.

2. Electronic transition energies

Table II summarizes the calculated adiabatic and vertical transition energies of the **1a**, **1b**, **2a**, **2b**, and **3a** conformers predicted by the SCS-CC2 method, together with the MS-CASPT2 transitions for **1a**. Both methods are in good agreement, which validates our computational approach. They predict that the S_1 state minimum has $^1\pi\pi^*$ character. The calculated adiabatic transition of **1a** is 31 534 cm^{-1} (SCS-CC2) and 31 831 cm^{-1} (MS-CASPT2), in excellent agreement with the experimental value of 31 510 cm^{-1}. The vertical excitation energy of the $^1\pi\pi^*$ state with the SCS-CC2 and MS-CASPT2 methods is 36 610 and 36 500 cm^{-1}, respectively. There are two low-lying $^1n\pi^*$ states which arise from excitations out of the oxygen and nitrogen lone pairs, whose vertical excitation energies are 7000-10 000 cm^{-1} higher. The structure of the $^1n_O\pi^*$ state was optimized at the TD-CAMB3LYP level. It is a minimum on S_2 with adiabatic energy of 37 597 cm^{-1} (MS-CASPT2 single point). The structure optimization of the $^1n_O\pi^*$

TABLE II. SCS-CC2 and MS-CASPT2 calculated adiabatic and vertical transition energies (in cm^{-1}) and electronic oscillator strengths f_{el} for five tautomers of 5,6-trimethylenecytosine (see Fig. 1).

		SCS-CC2/aug-cc-pVDZ				MS-CASPT2/ANO-L			
Tautomer	Transition	Adiab.	Vert.	f_{el}[a]		Adiab.	vert.[b]	f_{el}[a]	Expt.
1a	$^1\pi\pi^*$	31 534	36 610	0.091 8		31 831	36 500	0.1174	31 510
	$^1n\pi^*$		42 349	0.001 52		37 597[c]	43 580[d]	0.0410	
							46 288[e]	0.0032	
	(OP)					33 017[f]			
	$^3\pi\pi^*$	27 978	30 671			27 774[g]	31 217		24 020–25 140
	Ion	65 975			65 440				
1b	$^1\pi\pi^*$	31 483	36 580	0.091 8	31 510				
	$^1n\pi^*$		42 352	0.001 91					
	$^3\pi\pi^*$		30 654		24 020–25 140				
	Ion				65 440				
2a	$^1n\pi^*$	38 631[h]	43 035	0.006 08					
	$^1\pi\pi^*$	34 508	38 589	0.102					
	$^3\pi\pi^*$		35 415						
2b	$^1n\pi^*$	39 319[h]	43 631	0.006 58					
	$^1\pi\pi^*$	35 008	38 871	0.101	35 930				
	$^3\pi\pi^*$		35 446						
3a	$^1n\pi^*$		43 312	0.009 25					
	$^1\pi\pi^*$	41 401	41 862	0.250					
	$^3\pi\pi^*$		29 432						

[a]Vertical excitation from S_0 equilibrium geometry, length.
[b]At SCS-CC2 optimized geometry.
[c]$n_O\pi^*$ minimum optimized at the TD-CAMB3LYP level, S_1 energy 35 282 cm^{-1}.
[d]Mixed $n_O\pi^*/n_N\pi^*$ with predominant $n_N\pi^*$ character.
[e]Mixed $n_O\pi^*/n_N\pi^*$ with predominant $n_O\pi^*$ character.
[f]Optimized at the CASSCF level.
[g]Optimized at the TD-CAMB3LYP level.
[h]Not fully converged.

state did not converge with SCS-CC2 because it reached a region of S_2/S_1 degeneracy, which is consistent with the small S_2/S_1 energy gap found at the $^1n_O\pi^*$ minimum at the MS-CASPT2 level. Optimization of the $^1n_N\pi^*$ state at the CASSCF level leads to $(OP)_{Min}$, with an adiabatic energy of 33 017 cm^{-1}. The electronic configuration at this structure is analogous to that described in our previous work on 1-MCyt.[33]

The adiabatic transition energy of conformer **1a** is calculated to lie slightly above that of **1b**, differing by 51 cm^{-1} at the SCS-CC2 level. With this method, the $S_0 \rightarrow S_1$ transitions of the major tautomers **2b** and **2a** are calculated to be $^1\pi\pi^*$ and to lie at ~35 000 and ~34 500 cm^{-1}, respectively, or about 3500 cm^{-1} further to blue than the transitions of the **1a/1b** conformers. The lowest-energy electronic transition of the imino-keto tautomers **3a** and **3b** is predicted at 41 400 cm^{-1} and 40 970 cm^{-1}, respectively. This is above the experimental spectral range covered in this work. On the other hand, the lowest $^1\pi\pi^*$ transition of the **4** (N3H) tautomer is predicted to lie very close to that of the **1** (N1H) tautomer. However, tautomer **4** is calculated to be 5.5–5.8 kcal/mol less stable than tautomer **1**; hence, we do not expect this tautomer to be observable in the supersonic jet.

3. Ground- and excited-state structures

In the SCS-CC2 S_0 optimized structure of **1a**, the pyrimidinone framework is C_s symmetric, and the amino group and the trimethylene ring are bent slightly out of the ring plane. In the $^1\pi\pi^*$ excited state, the SCS-CC2 and TD-CAMB3LYP methods predict (i) a stronger pyramidalization of the amino group, (ii) an in-plane deformation of the pyrimidinone framework, and (iii) an out-of-plane bend at the C^6 atom (see Fig. 1 for the atom numbering). Figure 2 shows the SCS-CC2/aug-cc-pVDZ calculated geometries and geometry changes of TMCyt for both amino-keto N1H conformers. The TD-CAM-B3LYP optimized structure has similar out-of-plane deformations, see Fig. S1 in the supplementary material. This is in line with previous results for 1-MCyt,[33] for which both methods predict a substantial deplanarization at the $^1\pi\pi^*$ state minimum.

4. Interconversion between the 1a and 1b isomers

As shown in Table I, three correlated quantum-chemical methods (MP2, CC2, and SCS-MP2) predict the energy difference between conformers **1a** and **1b** to be very small (1–10 cm^{-1}). At the typical T_{vib} = 5–7 K in our supersonic jet expansions, the relative population of **1a** and **1b** should thus be within a factor of 2–3. Given the computed adiabatic transition frequencies of 31 534 cm^{-1} for **1a** and 31 483 cm^{-1} for **1b** (see Table II), we should observe two spectra that are mutually shifted by about 50 cm^{-1}. However, the R2PI and UV/UV holeburning spectra discussed below show only a *single* ground-state species. The reason for this is the

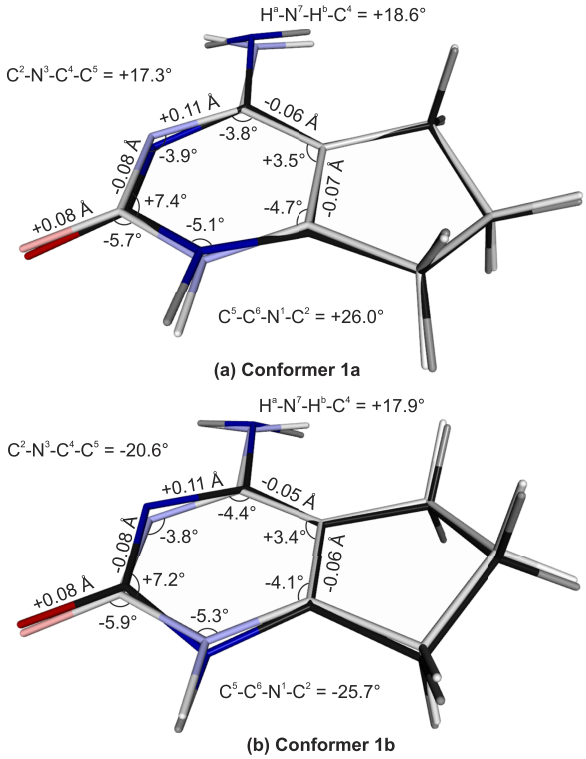

FIG. 2. SCS-CC2/aug-cc-pVDZ calculated geometries and geometry changes of amino-keto 5,6-trimethylenecytosine upon $^1\pi\pi^*$ excitation (ground state is light-colored and the $^1\pi\pi^*$ state is darker). Bond length changes ≥0.05 Å and bond angle changes ≥3° are indicated.

large-amplitude amino-inversion of TMCyt, which interconverts the conformers **1a** and **1b**.

In the S_0 state, the SCS-CC2/aug-cc-pVDZ calculated barrier height between **1a** and **1b** is ~30 cm^{-1}. We calculated the one-dimensional (1D) inversion potential at the same level by incrementing the H–N–C^4–N^3 and H–N–C^4–C^5 angles θ_{inv} from θ_{inv} = 0° by 5° in the positive and negative directions, relaxing all other internal coordinates at every point. The resulting 1D potential is shown in Fig. 3. The inversion eigenfunctions in this potential were calculated by numerically solving the 1D vibrational Schrödinger equation. The

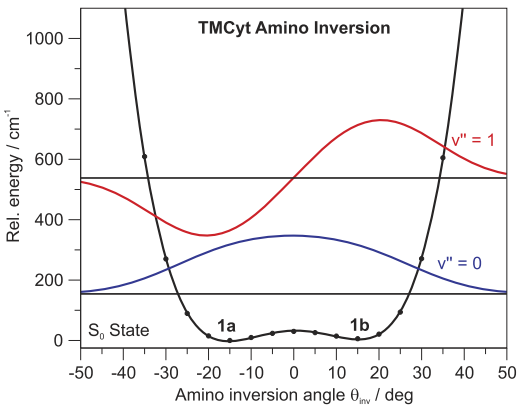

FIG. 3. SCS-CC2/aug-cc-pVDZ calculated S_0 state amino inversion potential energy curve of 5,6-trimethylenecytosine plotted along the inversion coordinate θ, see the text. The minima correspond to the **1a** and **1b** conformers, which are inequivalent; thus their energies differ by ~6 cm^{-1}. The **1a** → **1b** barrier height is 30 cm^{-1}. The wave functions of the v″ = 0 and v″ = 1 inversion levels are shown in blue and red.

reduced mass $\mu_{red,\theta}$ was determined by calculating the SCS-CC2/aug-cc-pVDZ amino-inversion imaginary normal-mode frequency at θ_{inv} = 0°; the central five points of the inversion potential were taken to represent the harmonic potential at this angle, and $\mu_{red,\theta}$ for the 1D calculation was fixed such that the calculated normal-mode and 1D frequencies in this harmonic potential were the same. Figure 3 shows that the lowest-energy v_{inv} = 0 level lies ~130 cm^{-1} above the barrier. Its wave function is delocalized over both the **1a** and **1b** geometries with its maximum near planarity (θ_{inv} = 0°). The fact that the vibrational ground state of TMCyt is quasiplanar (delocalized over both **1a** and **1b**) explains why the UV/UV holeburning spectra, discussed in Sec. III B, reflect the presence of a single ground-state species only. The second amino-inversion level v_{inv} = 1 lies 380 cm^{-1} higher. It will be collisionally cooled out in the supersonic expansion and will not be considered further.

In the S_0 state, the planar (C_s symmetric) structure of TMCyt is an index-2 stationary point. Normal-mode analysis at this point yields imaginary frequencies for both the NH_2 inversion and trimethylene-ring out-of-plane vibrations. The S_0-state barrier to planarity is 307 cm^{-1} at the SCS-CC2 level. In the $^1\pi\pi^*$ excited state, the barrier to planarity is much higher, 1297 cm^{-1}. Four imaginary frequencies are obtained at the C_s stationary point.

B. Experimental results: Two-color resonant two-photon ionization, UV/UV holeburning, and depletion spectra

Figure 4(a) shows a two-color R2PI overview spectrum of jet-cooled TMCyt in the 31 300–38 500 cm^{-1} range, recorded with the UV-OPO. The 0_0^0 transition of the amino-keto **1a/1b** tautomer is observed at 31 510 cm^{-1}. At the ~5 cm^{-1} resolution of the UV-OPO, vibronic bands are resolved up to +2100 cm^{-1} above the 0_0^0 band. The R2PI signal extends up 4000 cm^{-1} above, but due to the high density of vibronic excitations and the moderate ~5 cm^{-1} resolution, the band structure

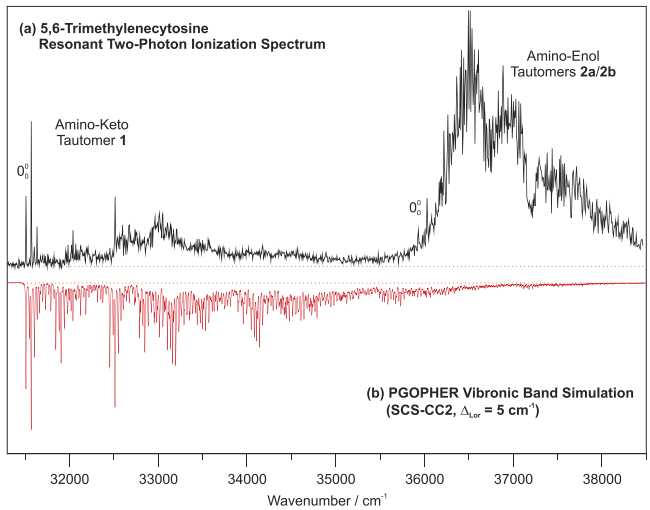

FIG. 4. (a) Two-color resonant two-photon ionization spectrum of jet-cooled TMCyt recorded with an UV-OPO as an excitation laser and (b) simulated vibronic spectra (with PGOPHER, plotted in the negative direction) based on the SCS-CC2/aug-cc-pVDZ S_0 and $S_1(^1\pi\pi^*)$ state calculations.

is washed out in this range. In Fig. 4(b), we show a PGOPHER vibronic band simulation based on SCS-CC2 structures and normal modes of TMCyt. They are seen to be in qualitative agreement with the R2PI spectrum and will be discussed in more detail in Sec. III F.

Starting at 35 930 cm^{-1} or 4420 cm^{-1} above the amino-keto 0_0^0 band in Fig. 4(a), further intense narrow-band absorption features are observed. Based on the SCS-CC2 calculations of Sec. III A 2, we assign these to the amino-enol tautomers **2b** predicted at 34 508 cm^{-1} and **2a** predicted at 35 008 cm^{-1}, see also Table II.

Figure 5(a) shows a higher-resolution 2C-R2PI spectrum of the amino-keto tautomers over the lowest 1500 cm^{-1} range (31 400–32 900 cm^{-1}) using a narrow-band frequency-doubled dye laser for excitation. Because of its 0.05 cm^{-1} bandwidth, the vibronic bands are much better resolved in this spectrum. Detailed vibronic assignments are given in Sec. III C. A high-resolution UV/UV holeburning spectrum is shown in Fig. 5(b) and was recorded with the burn laser at the intense band at $0_0^0 + 59$ cm^{-1}, marked with an asterisk in Fig. 5(a). It reproduces the 2C-R2PI spectrum in Fig. 5(a) in great detail. From this we conclude that all the observed vibronic bands originate from the ground-state level that gives rise to the transition at $0_0^0 + 59$ cm^{-1}. Figure 5(c) shows the corresponding UV/UV depletion spectrum in which the holeburning laser is scanned with the detection laser fixed at the intense $0_0^0 + 59$ cm^{-1} band. The UV/UV depletion spectrum also reproduces the R2PI spectrum, although the signal/noise ratio is lower than that in the UV holeburning spectrum. At 900 cm^{-1} above the electronic origin, the widths of the vibronic bands begin to increase, which indicates the onset of rapid non-radiative processes, see Sec. III F. Although no further bands can be observed in the depletion spectrum above +1000 cm^{-1}, the signal remains slightly below the baseline, indicating a constant depletion of the ion signal.

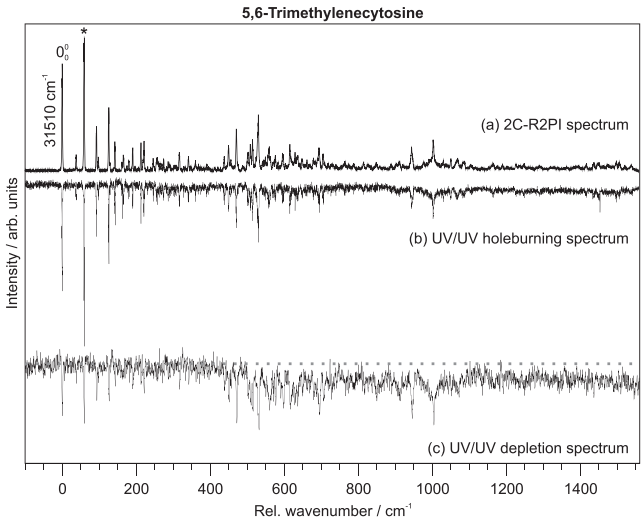

FIG. 5. (a) $S_0 \rightarrow S_1$ two-color resonant two-photon ionization spectrum of supersonic-jet cooled amino-keto 5,6-trimethylenecytosine (ionization at 245 nm). (b) UV/UV holeburning spectrum with the holeburning laser at the $0_0^0 + 59$ cm^{-1} band (marked with an asterisk). (c) UV/UV depletion spectrum with the detection laser fixed at the $0_0^0 + 59$ cm^{-1} band. The wavenumber scale is relative to the 0_0^0 band at 31 510 cm^{-1}.

C. Vibronic band assignments

We first attempted to assign the vibronic bands in the R2PI spectrum of TMCyt in Fig. 5(a) based on the SCS-CC2, CC2, and TD-B3LYP harmonic frequencies of the $^1\pi\pi^*$ state given in Table III. The lowest-frequency in-plane vibration is predicted to be $\nu_1' = 254$ cm^{-1} (SCS-CC2), $\nu_1' = 248$ cm^{-1} (CC2), or $\nu_1' = 262$ cm^{-1} (TD-B3LYP); hence, the vibronic bands below ~250 cm^{-1} must arise from out-of-plane vibrations. Experimentally, the two lowest-frequency bands at 38 cm^{-1} and 59 cm^{-1} cannot belong to the same progression, so we assign these as fundamentals of the lowest-frequency out-of-plane vibrations ν_1' and ν_2' (that is, as 1_0^1 and 2_0^1). Table III shows that the lowest two frequencies calculated with the SCS-CC2, CC2, and TD-B3LYP methods are two to three times larger. Previous experience with SCS-CC2, CC2, and TD-B3LYP excited-state calculations of cytosine derivatives and pyrimidinones has shown that while the in-plane S_1 state vibrational frequencies are well reproduced, the calculated out-of-plane vibrational frequencies are often 2-3 times higher than that observed experimentally.[6–8,31,33]

For the PGOPHER[44] vibronic band simulations (see Sec. II B), we therefore decreased the out-of-plane frequencies to the experimental values. Figures 6(a)–6(c) show the simulated vibronic bands in red for the 0–420, 420–870, and 870–1320 cm^{-1} sections of the spectrum and compare these to the high-resolution 2C-R2PI spectrum in black. We first fitted the S_1 state in-plane vibrational frequencies. The SCS-CC2 calculation predicts the lowest four in-plane fundamentals ν_6', ν_{11}', ν_{12}', and ν_{15}' at 254, 461, 472, and 618 cm^{-1}, respectively, see Table III. These normal-mode eigenvectors are shown in Fig. 7. The ν_{11}' and ν_{12}' normal-modes correspond to the ν_{6a}' and ν_{6b}' in-plane vibrations that are characteristic of the $S_0 \rightarrow S_1$ spectra of benzene and its derivatives. We therefore assigned the bands at 449 cm^{-1} and 471 cm^{-1} as 12_0^1 and 11_0^1, respectively, see Fig. 6(b); the order of these two vibrations was interchanged to obtain a better fit with the experimental R2PI spectrum. The 6_0^1 transition was fitted to the band at 257 cm^{-1}; its intensity is rather small and it does not contribute further to the spectrum. The band at 615 cm^{-1} was assigned to the 15_0^1 fundamental. The band at 944 cm^{-1} is assigned as the in-plane fundamental ν_{23}', as the overtone 11_0^2 had no intensity, see Fig. 6(c).

We then fitted the out-of-plane vibrations, see Fig. 6(a). The weak band at 38 cm^{-1} is assigned as the ν_1' fundamental. Since the ν_2' and ν_4' vibrations involve structural changes of the trimethylene ring, see Table III, and hardly appear in the simulation, the intense 59 cm^{-1} band is assigned as the 3_0^1 "butterfly" vibrational fundamental. The 3_0^2 overtone was fitted to the band at 126 cm^{-1}. The fundamentals of ν_5' and ν_7' were fitted to the bands at 93 cm^{-1} and 221 cm^{-1}, respectively. The out-of-plane normal-mode eigenvectors ν_1', ν_3', ν_5', and ν_7' are shown in Fig. 8. Note that the SCS-CC2, CC2, and TD-B3LYP harmonic frequencies in Table III differ from the fitted frequencies (Table IV) by a factor of 2–3, indicating that the S_1 state potential-energy surface is much flatter and more anharmonic along these coordinates than that predicted by the excited-state calculations.

TABLE III. CC2, TD-B3LYP, and SCS-CC2 calculated normal-modes and wavenumbers (in cm^{-1}) for the lowest $^1\pi\pi^*$ excited state of 5,6-trimethylenecytosine.

			Conformer **1a**			Conformer **1b**			
	Irrep.[a]	Description[b]	CC2 aVDZ	B3LYP TZVP	SCS-CC2 aVDZ	CC2 aVDZ	B3LYP TZVP	SCS-CC2 aVDZ	Expt.
ν_1	a''	Boat	90.9	95.7	76.6	91.7	108.3	67.3	37.6
ν_2	a''	Pyrimidine/five-ring twist	120.1	122.7	119.8	119.8	136.6	120.9	
ν_3	a''	Butterfly	157.8	170.5	146.6	156.2	212.8	145.9	59.2
ν_4	a''	γN_1/five-ring planarization	212.1	203.2	191.1	212.0	221.9	186.2	
ν_5	a''	$\gamma_{as}NH_2/\delta C_2O$	319.4	373.2	232.6	323.6	471.4	224.1	92.4
ν_6	a'	$\beta_{as}NH_2/\beta_{as}$five-ring	247.7	261.5	253.8	246.8	270.1	248.9	256.7
ν_7	a''	$\gamma_{as}NH_2/\gamma C_6$	326.5	403.6	288.0	270.2	448.6	274.9	221.0
ν_8	a''	$\gamma_s NH_2/\gamma C_5/\gamma C_6$	367.5	343.1	336.1	327.6	372.0	345.1	
ν_9	a''	$\gamma N_1H/\gamma C_4/\gamma_s$ NH_2	528.6	625.5	352.8	550.6	722.3	357.7	
ν_{10}	a''	$\gamma N_1/\gamma_{as}$ NH_2	269.2	301.8	434.7	377.6	287.6	425.2	
ν_{11}	a'	6a	455.3	473.2	461.4	454.8	471.4	466.4	470.5
ν_{12}	a'	$6b/\delta N_1H/\delta C_2O$	469.1	497.2	471.5	470.2	536.7	453.9	449.3
ν_{13}	a''	γN_1H	495.5	538.4	504.9	502.6	645.2/600.7	500.2	501.8
ν_{14}	a''	$6b?/\gamma_s NH_2/\gamma N_1H/\gamma C_4/\gamma C_5$	559.1	579.5	553.0	532.1	579.9	552.0	
ν_{15}	a'	$3/\delta N_1H$	603.2	640.2	617.7	603.0	640.9	618.0	615.1
ν_{16}	a''	$\gamma C_7H_2/\gamma C_8H_2/\gamma C_9H_2/\gamma_s NH_2$	628.5	670.1	636.5	633.2	680.6	639.9	
ν_{17}	a''	5	676.1	744.6	668.2	673.8	769.8	665.7	
ν_{18}	a''	NH_2 inversion	649.1	483.7	691.3	647.6	532.7	700.5	
ν_{19}	a'	$\delta N_1H/\delta N_1C_2N_3/\nu C_2O$	742.2	777.0	736.6	743.2	781.1	740.3	
ν_{20}	a'	$\delta N_1H/\nu N_1C_2/\nu N_3C_4/\beta_{as}NH_2$	1056.6	1090.9	771.1	1055.6		770.6	
ν_{21}	a''	Five-ring stretch/$\gamma C_7H_2/\gamma C_8H_2$	846.7	847.5	847.9	845.6	848.0	847.7	
ν_{22}	a'	$\gamma C_7H_2/\gamma C_9H_2/\delta C_8H_2$ shear/$\beta_{as}NH_2/\nu N_3C_4$	879.8	883.4	868.0	882.5	905.1	866.6	
ν_{23}	a'	$\beta_{as}NH_2/\delta N_1C_2N_3/\delta N_1H$	858.4	926.1	901.8	858.1	888.7	900.2	944.4
ν_{24}	a'	Five-ring stretch/νC_2O	913.1	901.2	912.9	912.5	925.0	912.4	
ν_{25}	a'	$\delta C_8/\delta C_8H$/five-ring deformation (as)	1006.1	997.1	999.6	1006.2	1000.8	999.2	
ν_{26}	a''	Five-ring planar./$\gamma C_7H_2/\gamma C_8H_2/\gamma C_9H_2/\delta C_6N_1C_2$	1033.7	1058.6	1025.0	1032.6	1073.0	1027.3	
ν_{27}	a''	Five-ring planar./$\gamma C_7H_2/\gamma C_8H_2/\gamma C_9H_2$	1030.1	1052.1	1034.0	1031.9	1065.4	1033.9	
ν_{28}	a'	$\nu C_2O/\beta_{as}NH_2/\delta C_7C_8C_9$	919.4	1105.9	1058.5	918.4	1092.4	1056.6	
ν_{29}	a'	δC_7H_2 shear/δC_8H_2 shear/δC_9H_2 shear	1113.8	1135.6	1119.2	1114.2	1171.6	1119.3	
ν_{30}	a'	$\delta N_1H/\delta C_7H_2/\delta_s C_9H_2/\delta_{as}C_8H_2$	1176.8	1210.9	1184.0	1176.5	1213.5	1183.2	
ν_{31}	a'	$\beta_{as}NH_2/\delta N_1H/\delta C_7H_2/\delta C_9H_2$	1185.4	1196.8	1194.1	1183.8	1193.3	1192.0	
ν_{32}	a'	$\delta_{as}C_7H_2/\delta_{as}C_8H_2/\delta_{as}C_9H_2$	1216.8	1230.0	1223.8	1218.5	1234.6	1224.9	
ν_{33}	a'	$\nu N_1C_6/\delta C_8H_a/\delta C_9H_a/\delta N_1H$	1231.8	1268.4	1233.3	1232.4	1155.7	1237.7	
ν_{34}	a'	$\delta_s C_7H_2/\delta_s C_8H_2/\delta N_1H/\nu C_6NH_2$	1325.8	1362.7	1273.1	1325.9	1360.4	1274.6	
ν_{35}	a'	$\delta_s C_9H_2/\delta_{as}C_8H_2/\delta N_1H$	1284.5	1313.4	1291.6	1284.5		1291.5	
ν_{36}	a'	$\delta_s C_7H_2/\beta_{as}NH_2$	1273.0	1299.8	1315.4	1272.2	1295.9	1313.8	
ν_{37}	a'	$\delta_s C_8H_a$	1311.6	1335.7	1328.0	1311.9		1326.7	
ν_{38}	a'	$\nu N_1C_2/\nu C_5C_6/\delta N_1H/\delta C_9H_2/\delta C_7H_2$	1393.8	1465.7	1392.1	1395.2	1180.8	1401.2	

[a]Irreducible representation in the C_s point group.

[b]Based on SCS-CC2/aug-cc-pVDZ eigenvectors; ν = stretching vibration; δ = in-plane bending vibration; γ = out-of-plane bending vibration; β_s = scissoring vibration; β_{as} = in-plane rocking vibration; γ_s = out-of-plane wagging vibration; γ_{as} = torsion vibration.

D. Photoionization efficiency curves

Figure 9 shows the photoionization efficiency (PIE) curves of the $S_1(^1\pi\pi^*)$ state, which were recorded at 0 ns delay of the ionization laser, and of a long-lived state, which was recorded at 50 ns delay. The PIE curve of the long-lived state shown in Fig. 9 is scaled according to the relative signal heights discussed in Sec. III E, where the T_1 ion signal reaches 25% of the S_1 signal when ionizing at 225 nm.

The PIE curve of the $S_1(^1\pi\pi^*)$ state in Fig. 9 exhibits a step-like ionization threshold at 33 930 ± 20 cm^{-1}, indicating that the geometry change between the $v' = 0$ level of the $S_1(^1\pi\pi^*)$ state and the $TMCyt^+$ ion ground state D_0 is small. The Franck-Condon factor for adiabatic ionization from the S_1 state is sufficiently large, so the adiabatic ionization energy (AIE) threshold can be observed. The sum of the $S_0 \rightarrow S_1$ 0_0^0 excitation energy of 31 510 cm^{-1} and the PIE threshold in Fig. 9 is 65 440 ± 20 cm^{-1}, giving an AIE = 8.114 ± 0.002 eV. The SCS-CC2 calculated AIE = 8.18 eV of tautomer **1a** is in good agreement with this value (see Table II).

The delayed-ionization PIE curve of the long-lived state shown in Fig. 9(b) is relatively noisy; since the UV spectrum of the TMCyt amino-enol forms begins around ~36 000 cm^{-1}, this contribution to the signal had to be subtracted. The PIE curve exhibits a gradual signal onset at 40 320 cm^{-1} followed by a slow rise. We interpret the long-lived state as the lowest triplet state T_1 and this slow onset as

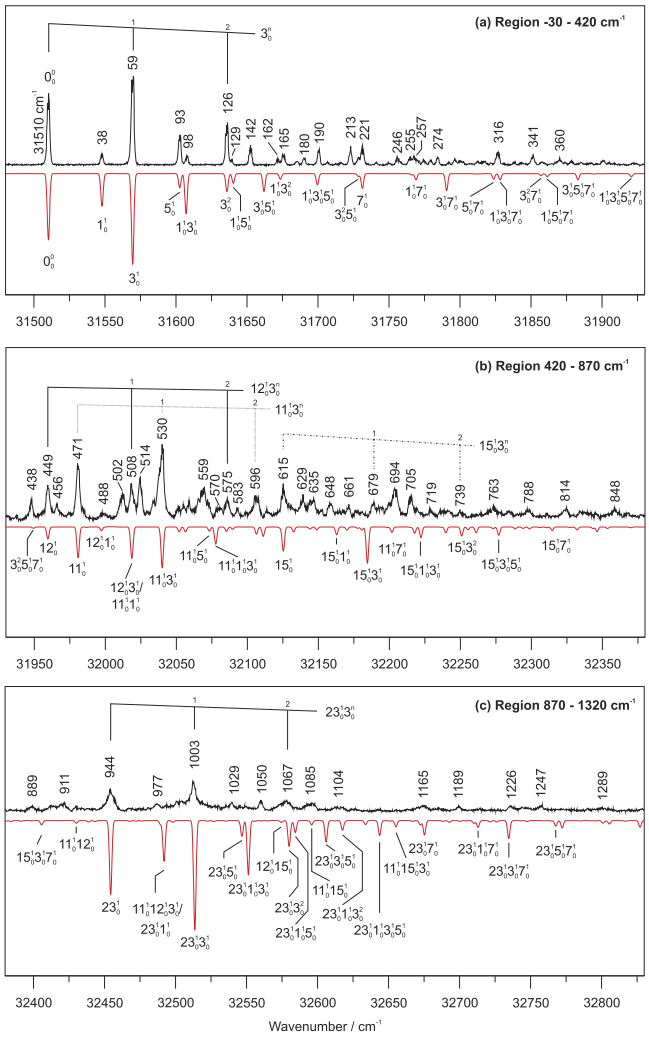

FIG. 6. 2C-R2PI spectrum of jet-cooled TMCyt (upper traces, in black) and PGOPHER simulated vibronic spectrum (lower red traces, plotted in the negative direction) for (a) the region –30–420 cm^{-1}, (b) the region 420–870 cm^{-1} (enhanced by factor 2), and (c) the region 870–1320 cm^{-1} (enhanced by factor 1.5). For details of the PGOPHER simulation see Fig. 4.

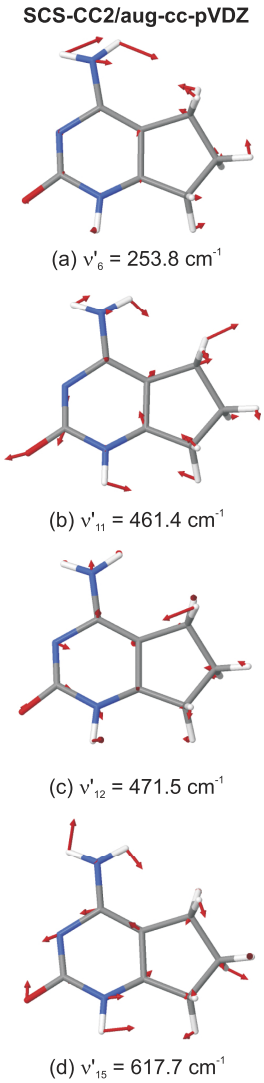

FIG. 7. SCS-CC2/aug-cc-pVDZ normal-mode eigenvectors of the four lowest-frequency $S_1(^1\pi\pi^*)$ in-plane vibrations of 5,6-trimethylenecytosine.

photoionization of the hot vibrational levels of T_1 that are formed by $S_1 \rightsquigarrow T_1$ intersystem crossing (ISC); the $S_1 \leftrightarrow T_1$ energy difference is converted to vibrational energy of the T_1 state during the ISC process. The signal onset at 40 320 cm^{-1} is thus interpreted as the lower limit to the AIE of the T_1 state. The upper limit to the AIE is estimated by back-extrapolation of the linear part of the PIE curve to the zero-signal line at 41 400 cm^{-1}. Subtracting these two values from the AIE of the $S_1(^1\pi\pi^*)$ state (65 440 ± 20 cm^{-1}) places the T_1 state between 24 020 cm^{-1} and 25 140 cm^{-1} above the S_0 ground state. The SCS-CC2 calculations (see Table II) support this assignment; the calculated adiabatic T_1 state adiabatic energy is ~27 800 cm^{-1}, whereas the alternative of a dark $^1n_O\pi^*$ state can be discarded because its estimated energy is much higher, 37 597 cm^{-1}, see Table II.

E. Ns pump/ionization delay scan measurements and nonradiative kinetics

We measured the excited-state lifetime and nonradiative kinetics of TMCyt using ns laser pump/delayed ionization measurements by ionizing at 225 nm. The convolution of the pulse widths of the pump and ionization laser yields a Gaussian instrument response function (IRF) with a full width at half-maximum (FWHM) of 4.2 ns. We modeled the S_1 ($^1\pi\pi^*$) state kinetics as

$$\frac{d[S_1]}{dt} = -(k_{rad}^{S_1} + k_{IC}^{S_1} + k_{ISC}^{S_1}) \cdot [S_1], \quad (1)$$

where k_{rad} is the $S_1 \rightarrow S_0$ radiative decay rate. The SCS-CC2 calculated oscillator strength of TMCyt is $f_{el} = 0.0918$, giving $\tau_{rad} \sim 12$ ns or $k_{rad} = 8.3 \cdot 10^7$ s^{-1}. This value is in good agreement with the $\tau_{rad} = 13$ ns that Zgierski *et al.* estimated from the integrated $S_0 \rightarrow S_1$ absorption spectrum of TMCyt in aqueous solution.[26] The S_1 state is assumed to decay nonradiatively to S_0 by internal conversion (IC) with the rate constant $k_{IC}^{S_1}$ and by intersystem crossing (ISC) to the T_1 state with the rate constant $k_{ISC}^{S_1}$. T_1 is assumed to relax to S_0 by $T_1 \rightsquigarrow S_0$ reverse ISC and also by phosphorescence; these two pathways are combined into a single rate constant k_T,

$$\frac{d[T_1]}{dt} = k_{ISC}^{S_1} \cdot [S_1] - k_T \cdot [T_1]. \quad (2)$$

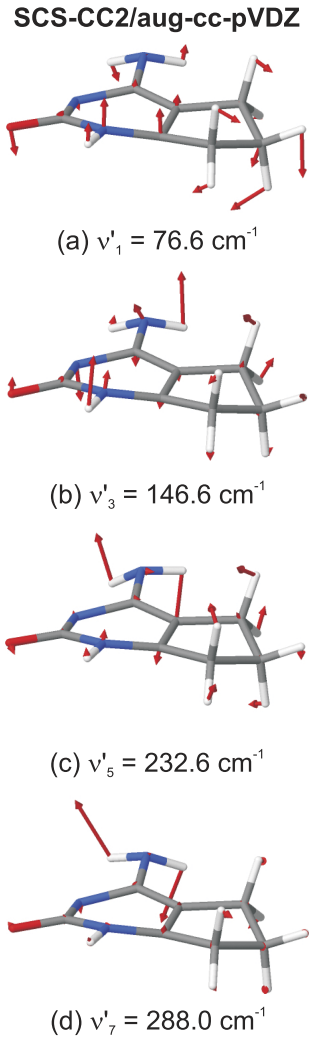

FIG. 8. SCS-CC2/aug-cc-pVDZ normal-mode eigenvectors of the $S_1(^1\pi\pi^*)$ state out-of-plane modes of 5,6-trimethylenecytosine.

However, k_T is very low ($<5 \cdot 10^6$ s) and we cannot determine it by delay measurements on the ~50 ns time scale, so it is set to zero. The simulated time-dependent concentrations $[S_1]$ and $[T_1]$ were convoluted with the IRF and were least-squares fitted to the experimental pump/ionization signal traces.

Note that because of the 4.2 ns width of the IRF, which is similar to the inverse of the k_{IC} and k_{ISC} rate constants, the ratio of the ionization efficiencies of molecules in the S_1 and T_1 states, $\sigma_{ion}(S_1):\sigma_{ion}(T_1)$, can only be estimated within certain limits discussed below. If the width of the two laser pulses was significantly shorter than the inverse of the k_{IC} and k_{ISC} rates, then the experimental pump/ionization transient would exhibit a much more intense S_1 signal that would peak close to 100% on the scale as shown in Fig. 10, and the observed S_1:T_1 signal ratio would be correspondingly larger.

In Figs. 10(a)–10(c), we show the experimental pump/ionization transient with excitation at the 0_0^0 band and ionization at 225 nm, marked by a dashed vertical line in Fig. 9. This transient is fitted for three different assumptions for the ionization efficiency ratio $\sigma_{ion}(S_1):\sigma_{ion}(T_1)$. In Fig. 10(a), we assume $\sigma_{ion}(S_1):\sigma_{ion}(T_1) = 1$, giving the nonradiative rate constants $k_{IC} = 2.2 \cdot 10^8$ s^{-1} and $k_{ISC} = 4.1 \cdot 10^7$ s^{-1}. Note, however, that this ratio is unrealistically low since ionization

TABLE IV. Experimental $^1\pi\pi^*$ state vibrational wavenumbers of 5,6-trimethylenecytosine (in cm^{-1}) measured by 2C-R2PI spectroscopy.

Assignment	Frequency		Frequency		Frequency
Region I		Region II		Region III	
0_0^0	(31 510.2)	ν'_{12}	449.3	$\nu'_{11}+\nu'_{12}$	919.8
ν'_1	37.7	ν'_{11}	470.6	ν'_{23}	944.4
ν'_3	59.3	$\nu'_{12}+\nu'_1$	488.2	$\nu'_{11}+\nu'_{12}+\nu'_3$	976.5
ν'_5	92.5			$\nu'_{23}+\nu'_3$	1002.5
$\nu'_1+\nu'_3$	97.7	$\nu'_{12}+\nu'_3$	508.0		
$2\nu'_2$	125.7	$\nu'_{11}+\nu'_1$	514.1	$\nu'_{11}+\nu'_{12}+2\nu'_3$	1049.7
$\nu'_1+\nu'_5$	128.7	$\nu'_{11}+\nu'_3$	529.6	$\nu'_{23}+2\nu'_3$	1067.1
$\nu'_3+\nu'_5$	142.4			$\nu'_{11}+\nu'_{15}$	1085.1
$\nu'_1+2\nu'_3$	165.4	$\nu'_{12}+2\nu'_3$	575.6	$\nu'_{23}+\nu'_7$	1164.5
$\nu'_1+\nu'_3+\nu'_5$	190.3	$\nu'_{11}+2\nu'_3$	596.0	$\nu'_{23}+\nu'_3+\nu'_7$	1225.6
?	212.7	ν'_{15}	615.1	$\nu'_{12}+\nu'_{23}$	1392.5
$2\nu'_3+\nu'_5$	218.4			$\nu'_{11}+\nu'_{23}$	1415.8
ν'_7	221.0	$\nu'_{15}+\nu'_3$	678.7	$\nu'_{12}+\nu'_{23}+\nu'_1$	1436.0
$\nu'_3+\nu'_7$	274.1	$\nu'_{11}+\nu'_7$	693.9		1447.0
		$\nu'_{15}+2\nu'_3$	739.4		1473.8

at 225 nm is 10 000 cm^{-1} above the S_1 ionization threshold but only 2700 cm^{-1} above the T_1 ionization threshold. For the fit in Fig. 10(b), we assume that the ionization efficiency ratio $\sigma_{ion}(S_1):\sigma_{ion}(T_1) = 4$, which is the *apparent* experimental ratio between the S_1 and T_1 ion signals at 225 nm shown

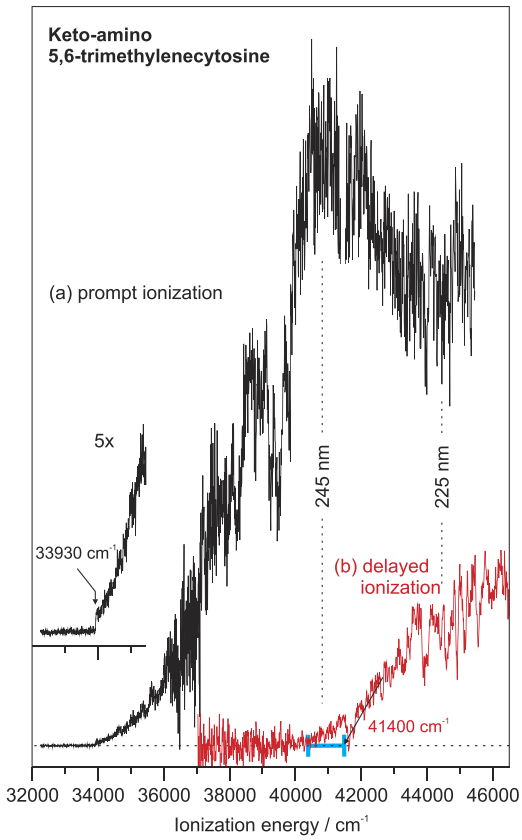

FIG. 9. Photoionization efficiency curves of 5,6-trimethylenecytosine following excitation at the S_1 0_0^0 band (a) with prompt ionization (0 ns delay); the step-like adiabatic photoionization threshold is shown in the inset (5x). (b) PIE curve with the ionization laser delayed by 50 ns, relative to the excitation. The uncertainty of the T_1 photoionization threshold is indicated with a blue bar.

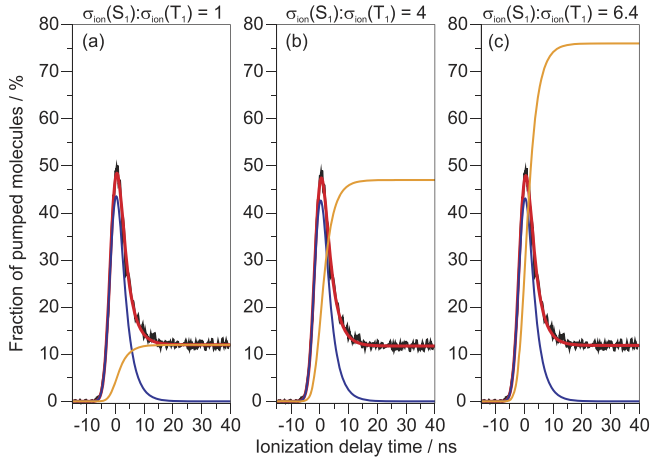

FIG. 10. Ns laser excitation/delayed ionization lifetime measurements of TMCyt (in black). Excitation at the 0_0^0 band, ionization at 225 nm. The kinetic fits assume that the ratios of S_1 and T_1 ionization cross sections are (a) 1:1, (b) 4:1, and (c) 6.4:1, for details see the text. The S_1 state signal contribution is plotted in blue and that of the T_1 state is in yellow; the fit of the total ion signal is in red.

in Fig. 9 and between the ion signals at 0 ns delay and 40 ns delay shown in Fig. 10. This fit gives the nonradiative rate constants $k_{IC} = 9.8 \cdot 10^7$ s^{-1} and $k_{ISC} = 1.6 \cdot 10^8$ s^{-1}. If—as the other limiting case—we assume k_{IC} to be zero and fit k_{ISC} and the $\sigma_{ion}(S_1)$:$\sigma_{ion}(T_1)$ ratio, we obtain the fit curves shown in Fig. 10(c). The resulting $\sigma_{ion}(S_1)$:$\sigma_{ion}(T_1) = 6.4$ is the maximum possible ratio, and the fitted $k_{ISC} = 2.6 \cdot 10^8$ s^{-1} is an upper limit for the ISC rate.

These IC and ISC rate constants of TMCyt can be compared to those of 1-MCyt, which are $k_{IC} = 2 \cdot 10^9$ s^{-1} and $k_{ISC} = 2 \cdot 10^8$ s^{-1} near the $S_1(v' = 0)$ level.[33] The main difference lies in the decrease of k_{IC} by a factor of 10–20. The ISC rate constant probably changes little upon rigidization of the pyrimidinone, but the uncertainty is large. Thus the increase in excited-state lifetime at the 0_0^0 band upon clamping the C^5–C^6 bond originates mainly from the decrease of the IC rate.

The pump/ionization transients were also measured at an ionization wavelength of 245 nm, which is the same wavelength as used to record the 2C-R2PI spectra. The measured 0_0^0 band transient was well fitted with the three sets of k_{IC} and k_{ISC} constants that correspond to Figs. 10(a)–10(c). However, Fig. 9 shows that ionization of the T_1 state at 245 nm is very inefficient; thus, the $\sigma_{ion}(S_1)$:$\sigma_{ion}(T_1)$ ratio was refitted and is 15.5 times larger that for ionization at 225 nm. These fits are shown in Figs. S3(a)–S3(c) of the supplementary material. Ns pump/ionization transients were also measured for the bands at $0_0^0 + 530$, $0_0^0 + 1174$, and $0_0^0 + 1646$ cm^{-1}, but only with ionization at 245 nm, see Figs. S3(d)–S3(f) of the supplementary material. These transients were fitted with a fixed $\sigma_{ion}(S_1)$:$\sigma_{ion}(T_1) = 15.5$, which corresponds to assuming $\sigma_{ion}(S_1)$:$\sigma_{ion}(T_1) = 1$ and T_1 states at 225 nm. All fitted k_{IC} and k_{ISC} values assuming $\sigma_{ion}(S_1)$:$\sigma_{ion}(T_1) = 1$ at 225 nm are collected in Table V.

Summarizing, one sees that although the ns time resolution of the pump/ionization transient measurement and the unknown ratio $\sigma_{ion}(S_1)$:$\sigma_{ion}(T_1)$ lead to considerable uncertainty, k_{IC} is determined within a factor of 2.5 between $k_{IC} = 9.8 \cdot 10^7$ and $2.2 \cdot 10^8$ s^{-1}. Similarly, the limits of the

TABLE V. Internal conversion (IC) and intersystem crossing (ISC) rate constants, decay lifetimes, fluorescence quantum yields Φ_{fl}, and ISC quantum yields Φ_{ISC}, from fits to the ns excitation/ionization transients in Fig. 10 and Fig. S3 of the supplementary material, assuming the relative ionization efficiencies of the S_1 and T_1 states at 225 nm to be equal.

Band (cm^{-1})	$k_{IC}/10^8$ (s^{-1})	$k_{ISC}/10^7$ (s^{-1})	Lifetime τ> (ns)	Φ_{fl}	Φ_{ISC}
0_0^0	2.2	4.1	2.9 ± 0.2	0.24	0.12
+530	3.4	6.6	2.0 ± 0.3	0.17	0.13
+1174	4.6	9.4	1.6 ± 0.2	0.13	0.15
+1646	12	12	0.7 ± 0.4	0.06	0.09

ISC rate constant are determined within a factor of four as $k_{ISC} = 4.1 \cdot 10^7$ to $1.6 \cdot 10^8$ s^{-1}. For all three fits, the lifetime at the 0_0^0 band is $\tau = 2.9$ ns. Given the calculated radiative rate constant $k_{rad} = 8.3 \cdot 10^7$ s^{-1} and that $\tau = 1/(k_{rad} + k_{ISC} + k_{IC})$, one finds that the fluorescence quantum yield of TMCyt is $\Phi_{fl} = 24\%$. This value does not depend on the exact k_{IC} and k_{ISC} rate constants. For TMCyt in room-temperature aqueous solution, Zgierski *et al.* determined $\Phi_{fl} \sim 10\%$ from the lifetime of $\tau = 1.2$ ns.[26] The fact that the fluorescence quantum yield at room temperature is lower than that at the low temperature in the supersonic jet is very reasonable and to be expected from the increase of k_{IC} with increasing vibrational energy, as is documented in Table V.

F. The $S_1 \leftrightarrow S_0$ conical intersections

In contrast to the $S_0 \rightarrow S_1$ vibronic spectra of Cyt and its derivatives 1-MCyt, 5-MCyt, and 5-FCyt,[6–8,33] which exhibit sharp break-offs at 450–1200 cm^{-1} above the 0_0^0 bands, indicating the onset of an ultrafast process, the $S_0 \rightarrow S_1$ 2C-R2PI spectrum of TMCyt **1a**/**1b** extends up to 4400 cm^{-1} above the 0_0^0 band and does not show a spectral break-off. The vibronic bands either merge or become diffuse at ~2100 cm^{-1} above the 0_0^0 band of the amino-keto tautomer. To investigate the reason for the broadening, we modeled the complete vibronic spectrum for TMCyt using PGOPHER 8.0;[44] the simulated spectrum is shown in Fig. 4(b). In addition to the nine optically active vibrational modes ν'_1, ν'_3, ν'_5, ν'_7, ν'_6, ν'_{11}, ν'_{12}, ν'_{15}, and ν'_{23} that were employed for the simulation in Fig. 6 in Sec. III C, we included the fundamental excitations of all vibrations with calculated Franck-Condon factors >15% of the 0_0^0 band. These are the in-plane vibrations ν'_{33}, ν'_{39}, ν'_{43}, ν'_{44}, and ν'_{45}, and the ν'_8 out-of-plane vibration. These frequencies were *not* fitted to experimental transitions but were taken from the SCS-CC2 calculations. The overtones and combination tones of these six vibrations could not be included because of the limited array sizes of PGOPHER.

A Gaussian line shape with a FWHM of 5 cm^{-1} was employed, reflecting the bandwidth of the UV-OPO. When setting the Lorentzian linewidth contribution Δ_{Lor} to zero, the simulated spectrum exhibits resolved vibronic bands up to +4400 cm^{-1}. If we include a Lorentzian linewidth contribution $\Delta_{Lor} = 5$ cm^{-1} in the simulation, which corresponds to a lifetime of 1 ps, we see in Fig. 4(b) that the bands broaden and merge into a semi-continuous background that is similar to the experimental spectrum in Fig. 4(a). This suggests

that the broadening of the spectrum at excess energies above +2100 cm^{-1} does not reflect just spectral congestion but arises from a decrease in the excited-state lifetime.

To account for the additional broadening observed in the experimental spectrum, we have calculated the two most energetically favorable excited-state decay paths that are analogous to those for cytosine and 1-MCyt.[10,16,18,19,46–49] According to expectations and in line with the calculations of Zgierski *et al.*,[26] the access to the ethylene-type intersection is hindered by the trimethylene modification. The calculated energy of the $(Eth)_X$ CI is approximately 6800 cm^{-1} relative to the 0_0^0 transition. The path from $^1\pi\pi^*_{Min}$ to that CI has a sloped topology, and the barrier for the decay is given by the energy of the CI itself, see Fig. S2 in the supplementary material.

The energetically favored decay path involves out-of-plane deformation of N^3 and the amino group. The calculated energy profile along this path is shown in Fig. 11. The path leads from the $S_1(^1\pi\pi^*_{Min})$ structure through a transition state (TS) to a second minimum, $(OP)_{Min}$, which is similar to that previously characterized for Cyt and 1-MCyt.[10,16,18,19,46–49] The MS-CASPT2 barrier over the TS is 1935 cm^{-1}, and the energy of $(OP)_{Min}$ relative to $^1\pi\pi^*_{Min}$ is 1056 cm^{-1}. The decay path leads further to the $(OP)_X$ CI, which has a relative energy of approximately 4300 cm^{-1}. The $(OP)_{Min}$ and $(OP)_X$ structures are characterized by a large out-of-plane bending of N^3, with a C^2–N^3–C^4–C^5 angle of 60.1° and 58.2°, respectively. The ring puckering and out-of-plane bending of the amino group also increase from $(OP)_{Min}$ to $(OP)_X$ (see the O^8–C^2–N^1–C^6 and N^7–C^4–C^5–C^6 angles in Fig. 12), which is consistent with the decay path where $(OP)_{Min}$ lies before the $(OP)_X$ CI.

The fact that broadening of the vibronic bands in the R2PI spectrum sets in at around ~2100 cm^{-1}, but a semi-continuous spectrum continues up to 4400 cm^{-1} above the electronic origin, is in qualitative agreement with the calculated decay path topology. We interpret the additional broadening beyond ~2100 cm^{-1} due to the coupling between the vibrations belonging to the $S_1(\pi\pi^*)$- and the OP_{Min}-minima below the barrier. The density of vibronic states belonging to both minima rises enormously when the energy exceeds this barrier (MS-CASPT2 barrier 1935 cm^{-1}). The

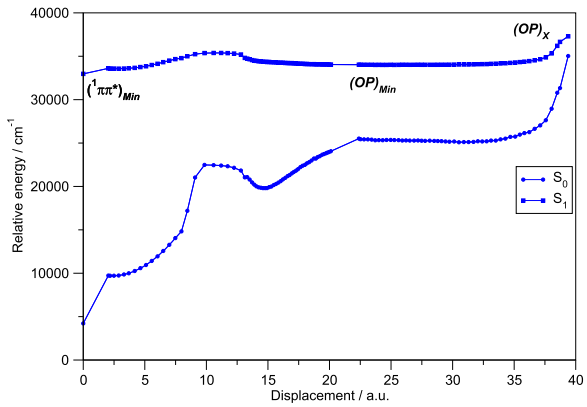

FIG. 11. MS-CASPT2 energy profile of the S_0 and S_1 singlet states along the CASSCF optimized paths for radiationless decay on S_1 from $(^1\pi\pi^*)_{Min}$ to $(OP)_X$ through $(OP)_{Min}$. Blue squares: S_1; blue dots: S_0.

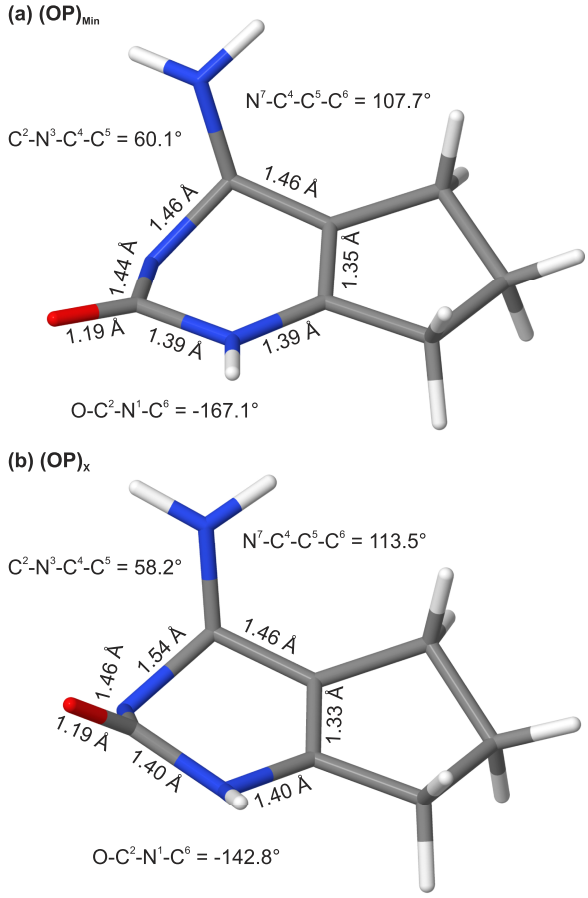

FIG. 12. (a) Structure of the $(OP)_{Min}$ minimum in the S_1 energy surface of 5,6-trimethylenecytosine. (b) Structure of the $(OP)_X$ conical intersection.

semi-continuous spectrum that reaches up to at least 4400 cm^{-1} is also in good agreement with the calculated CI at 4300 cm^{-1}.

IV. CONCLUSIONS

We have measured the UV vibronic spectra of jet-cooled amino-keto 5,6-trimethylenecytosine (TMCyt) using two-color resonant two-photon ionization, UV/UV holeburning, and depletion spectroscopies. The 0_0^0 band is identified at 31 510 cm^{-1}. The lowest 400 cm^{-1} of the $S_0 \rightarrow S_1$ spectrum is dominated by fundamentals, overtone excitations, and combination bands of four out-of-plane vibrations. Based on the energetic sequence of the SCS-CC2 calculated vibrational frequencies and on their predicted Franck-Condon factors, we assign these as ν'_1, ν'_3, ν'_5, and ν'_7. Similar to the spectra of cytosine, 5-methylcytosine, and 5-fluorocytosine,[6–8] the longest vibronic progression is observed for the butterfly vibration ν'_3. Combination progressions in ν'_3 are also built on the in-plane vibrational fundamentals ν'_{11}, ν'_{12}, ν'_{15}, and ν'_{23}. In contrast to unsubstituted cytosine, whose $S_0 \rightarrow S_1$ spectrum breaks off above ~500 cm^{-1}, the R2PI spectrum of TMCyt extends to ~4400 cm^{-1} above, with more than 100 resolved vibronic bands. This is the most extended $S_0 \rightarrow S_1$ spectrum of any cytosine derivative measured so far. We have also observed the R2PI spectra of the amino-enol tautomers **2a** and **2b** starting at ~36 000 cm^{-1}, but these will be discussed elsewhere.

Sharp vibronic bands can be observed up to +2100 cm^{-1} above the 0_0^0 band. Hence, bridging of the C^5–C^6 bond with the trimethylene ring strongly raises the barrier to the ethylene-type $(Eth)_X$ conical intersection. Above +2100 cm^{-1}, a semi-continuous R2PI spectrum is observed up to at least +4400 cm^{-1}. The vibronic band simulation performed with the PGOPHER program[44] nicely reproduces the vibronic band structure and intensities of the R2PI spectrum up to +1320 cm^{-1}. Towards higher frequencies, the simulations predict resolved vibronic transitions, whereas in the R2PI spectrum, an increased density of bands leads to an intense continuous signal.

From a mechanistic perspective, our computational work shows that, by blocking the twist of the C^5–C^6 bond, we not only change the energetically favored decay path but also the topology. In Cyt and 1-MCyt, the decay path leads from the $^1\pi\pi^*$ minimum via a TS to the ethylene-type $(Eth)_X$ CI. The CI can be reached as soon as enough energy is available to go over the TS, and this is observed as a sharp break-off of the R2PI spectrum above ~500 cm^{-1} in these systems. In contrast, in TMCyt, the lowest CI is the amino out-of-plane bend $(OP)_X$ and the $(Eth)_X$ CI is raised ~6800 cm^{-1} above the S_1 vibrationless level. The path to $(OP)_X$ involves an additional minimum that lies before the intersection. As a consequence, the R2PI spectrum does not completely break off when enough energy is available to go over the TS. This suggests that the broad, shapeless spectral region between 2100 and 4300 cm^{-1} is a signature of the calculated topology.

The excited-state lifetime of amino-keto TMCyt at the 0_0^0 band is τ = 2.9 ns, which is a fourfold increase relative to that of cytosine at its 0_0^0 band. Additionally, the lifetime τ drops off much more slowly with increasing vibrational excess energy, being τ = 1.6 ns even at a vibrational excess energy E_{exc} = 1174 cm^{-1}. From the calculated S_1 state radiative lifetime and experimental lifetime τ, we infer that the fluorescence quantum yield at the $v' = 0$ level is Φ_{fl} = 24%, which makes TMCyt the strongest fluorescing cytosine derivative in the gas phase known to date. Φ_{fl} drops to ~6% at E_{exc} = 1646 cm^{-1}. These fluorescence lifetimes and quantum yields are in qualitative agreement with the τ = 1.2 ns and $\Phi_{fl} \sim 10\%$ values that Zgierski *et al.* determined for TMCyt in room-temperature aqueous solution.[26] The availability of a strongly fluorescent gas-phase cytosine derivative opens exciting new research opportunities based on fluorescence measurements.

SUPPLEMENTARY MATERIAL

See supplementary material for the synthesis of 5,6-trimethylenecytosine, additional computational details on the MS-CASPT2 calculations, and additional ns pump/ionization transients.

ACKNOWLEDGMENTS

The Bern group acknowledges support by the Schweizerische Nationalfonds (Project No. 200020-152816). L.B. acknowledges financial support from the Spanish Ministerio de Economía y Competitividad (CTQ2015-69363-P) and the Generalitat de Catalunya (2014SGR-2012).

[1] H. Kang, K. T. Lee, B. Jung, Y. J. Ko, and S. K. Kim, J. Am. Chem. Soc. **124**, 12958 (2002).
[2] C. Canuel, M. Mons, F. Piuzzi, B. Tardivel, I. Dimicoli, and M. Elhanine, J. Chem. Phys. **122**, 074316 (2005).
[3] S. Ullrich, T. Schultz, M. Z. Zgierski, and A. Stolow, Phys. Chem. Chem. Phys. **6**, 2796 (2004).
[4] K. Kosma, C. Schröter, E. Samoylova, I. V. Hertel, and T. Schultz, J. Am. Chem. Soc. **131**, 16939 (2009).
[5] J. W. Ho, H.-C. Yen, W.-K. Chou, C.-N. Weng, L.-H. Cheng, H.-Q. Shi, S.-H. Lai, and P.-Y. Cheng, J. Phys. Chem. A **115**, 8406 (2011).
[6] S. Lobsiger, M. A. Trachsel, H. M. Frey, and S. Leutwyler, J. Phys. Chem. B **117**, 6106 (2013).
[7] M. A. Trachsel, S. Lobsiger, and S. Leutwyler, J. Phys. Chem. B **116**, 11081 (2012).
[8] S. Lobsiger, M. A. Trachsel, T. Den, and S. Leutwyler, J. Phys. Chem. B **118**, 2973 (2014).
[9] S. Blaser, M. A. Trachsel, S. Lobsiger, T. Wiedmer, H.-M. Frey, and S. Leutwyler, J. Phys. Chem. Lett. **7**, 752 (2016).
[10] N. Ismail, L. Blancafort, M. Olivucci, B. Kohler, and M. Robb, J. Am. Chem. Soc. **124**, 6818 (2002).
[11] M. Merchán and L. Serrano-Andrés, J. Am. Chem. Soc. **125**, 8108 (2003).
[12] K. Tomic, J. Tatchen, and C. M. Marian, J. Phys. Chem. A **109**, 8410 (2005).
[13] M. Z. Zgierski, S. Patchkovskii, T. Fujiwara, and E. C. Lim, J. Chem. Phys. **123**, 081101 (2005).
[14] L. Blancafort, B. Cohen, P. M. Hare, B. Kohler, and M. A. Robb, J. Phys. Chem. A **109**, 4431 (2005).
[15] M. Merchán, R. Gonzalez-Luque, T. Climent, L. Serrano-Andrés, E. Rodríguez, M. Reguero, and D. Peláez, J. Phys. Chem. B **110**, 26471 (2006).
[16] K. A. Kistler and S. Matsika, J. Phys. Chem. A **111**, 2650 (2007).
[17] K. A. Kistler and S. Matsika, J. Chem. Phys. **128**, 215102 (2008).
[18] H. R. Hudock and T. J. Martínez, ChemPhysChem **9**, 2486 (2008).
[19] M. Barbatti, A. J. A. Aquino, J. J. Szymczak, D. Nachtigallova, and H. Lischka, Phys. Chem. Chem. Phys. **13**, 6145 (2011).
[20] R. Improta, F. Santoro, and L. Blancafort, Chem. Rev. **116**, 3540 (2016).
[21] L. Serrano-Andrés and M. Merchán, J. Photochem. Photobiol. C **10**, 21 (2009).
[22] M. Kotur, T. C. Weinacht, C. Zhou, K. A. Kistler, and S. Matsika, J. Chem. Phys. **134**, 184309 (2011).
[23] J. M. Pecourt, J. Peon, and B. Kohler, J. Am. Chem. Soc. **122**, 9348 (2000).
[24] J. Peon and A. H. Zewail, Chem. Phys. Lett. **348**, 255 (2001).
[25] T. Gustavsson, A. Sharonov, and D. Markovitsi, Chem. Phys. Lett. **351**, 195 (2002).
[26] M. Z. Zgierski, T. Fujiwara, W. G. Kofron, and E. C. Lim, Phys. Chem. Chem. Phys. **9**, 3206 (2007).
[27] D. Berry, K.-Y. Yung, D. S. Wise, A. D. Sercel, W. H. Pearson, H. Mackie, J. B. Randolph, and R. L. Somers, Tetrahedron Lett. **45**, 2457 (2004).
[28] K. C. Thompson and N. Miyake, J. Phys. Chem. B **109**, 6012 (2005).
[29] S. J. O. Hardman, S. W. Botchway, and K. C. Thompson, Photochem. Photobiol. **84**, 1473 (2008).
[30] Q. E. Thompson, J. Am. Chem. Soc. **80**, 5483 (1958).
[31] S. Lobsiger, H.-M. Frey, S. Leutwyler, P. Morgan, and D. Pratt, J. Phys. Chem. A **115**, 13281 (2011).
[32] R. K. Sinha, S. Lobsiger, M. Trachsel, and S. Leutwyler, J. Phys. Chem. A **115**, 6208 (2011).
[33] M. A. Trachsel, T. Wiedmer, S. Blaser, H.-M. Frey, Q. Li, S. Ruiz-Barragan, L. Blancafort, and S. Leutwyler, J. Chem. Phys. **145**, 134307 (2016).
[34] N. Forsberg and P. A. Malmqvist, Chem. Phys. Lett. **274**, 196 (1997).
[35] G. Ghigo, B. O. Roos, and P. A. Malmqvist, Chem. Phys. Lett. **396**, 142 (2004).
[36] C. González and H. B. Schlegel, J. Phys. Chem. **94**, 5523 (1990).
[37] P. Celani, M. A. Robb, M. Garavelli, F. Bernardi, and M. Olivucci, Chem. Phys. Lett. **243**, 1 (1995).
[38] S. Ruiz-Barragan, M. A. Robb, and L. Blancafort, J. Chem. Theory Comput. **9**, 1433 (2013).
[39] TURBOMOLE V6.4 2013, A Development of Universität Karlsruhe (TH) and Forschungszentrum Karlsruhe GmbH, 1989-2007, TURBOMOLE GmbH, available from http://www.turbomole.com, accessed May 19 2015.
[40] The thresholds for SCF and one-electron density convergence were set to 10^{-9} a.u. and 10^{-8} a.u., respectively. The convergence thresholds for all structure optimizations were set to 10^{-8} a.u. for the energy change, $6 \cdot 10^{-6}$ a.u. for the maximum displacement element, 10^{-6} a.u. for the maximum gradient element, $4 \cdot 10^{-6}$ a.u. for the RMS displacement, and 10^{-6} a.u. for the RMS gradient.

[41]M. J. Frisch, G. W. Trucks, H. B. Schlegel, G. E. Scuseria, M. A. Robb, J. R. Cheeseman, G. Scalmani, V. Barone, B. Mennucci, G. A. Petersson *et al.*, GAUSSIAN 09, Revision A.02, Gaussian, Inc., Wallingford, CT, 2009.
[42]G. Karlstrom, R. Lindh, P. A. Malmqvist, B. O. Roos, U. Ryde, V. Veryazov, P. O. Widmark, M. Cossi, B. Schimmelpfennig, P. Neogrady, and L. Seijo, Comput. Mat. Sci. **28**, 222 (2003).
[43]F. Aquilante, L. De Vico, N. Ferré, G. Ghigo, P.-A. Malmqvist, P. Neogrady, T. B. Pedersen, M. Pitonak, M. Reiher, B. O. Roos, L. Serrano-Andrés, M. Urban, V. Veryazov, and R. Lindh, J. Comput. Chem. **31**, 224 (2010).
[44]C. M. Western, PGOPHER 8.0, a program for simulating rotational, vibrational and electronic structure, University of Bristol, 2015, http://pgopher.chm.bris.ac.uk.
[45]G. Fogarasi, J. Mol. Struct. **413**, 271 (1997).
[46]L. Blancafort, J. Photochem. Photobiol. **83**, 603 (2007).
[47]A. Nakayama, Y. Harabuchi, S. Yamazaki, and T. Taketsugu, Phys. Chem. Chem. Phys. **15**, 12322 (2013).
[48]Q. S. Li and L. Blancafort, Photochem. Photobiol. Sci. **12**, 1401 (2013).
[49]A. Nakayama, S. Yamazaki, and T. Taketsugu, J. Phys. Chem. A **118**, 9429 (2014).